The electronic properties of the strained CdTe/ZnTe(001) superlattices

2002 J. Phys.: Condens. Matter 14 7835

(http://iopscience.iop.org/0953-8984/14/34/304)

INSTITUTE OF PHYSICS PUBLISHING JOURNAL OF PHYSICS: CONDENSED MATTER

J. Phys.: Condens. Matter **14** (2002) 7835–7851 PII: S0953-8984(02)35894-6

The electronic properties of the strained CdTe/ZnTe(001) superlattices

Nacir Tit[1,3] **and Amna Al-Zarouni**[2]

[1] The Abdus Salam International Centre for Theoretical Physics, PO Box 586, 34100 Trieste, Italy
[2] The Electrical Engineering Department, UAE University, PO Box 17551, Al-Ain, United Arab Emirates

E-mail: ntit@uaeu.ac.ae

Received 10 April 2002, in final form 19 July 2002
Published 15 August 2002
Online at stacks.iop.org/JPhysCM/14/7835

Abstract

The common-anion II–VI semiconductor superlattices (SLs) are characterized by a vanishing or a small valence-band offset (VBO). In the case of the lattice-mismatched SLs, the biaxial strain can drastically affect the splitting of the valence-band top states, and therefore be explored in designing type-I character SLs. In the present work, we used the sp^3s^* tight-binding method, with the inclusion of strain and spin–orbit coupling effects, to investigate the electronic band structures of the strained CdTe/ZnTe(001) SLs versus the biaxial strain, layer thicknesses and VBO. Our results show that the electron is always confined within the CdTe slabs, whereas the hole behaviour controls the whole SL character. Our theoretical results are compared to the photoluminescence experiments and shown to be consistent with the strain morphology along the SL growth direction as well as the optical and structural qualities of the experimental samples.

1. Introduction

Recently, there has been a prominent growing interest in the II–VI semiconductor heterostructures because of their unique optical and electrical properties [1]. These compound semiconductors have a very wide variety of bandgap values (mostly *direct*) ranging from zero of the semimetal HgTe to 3.7 eV of ZnS. Moreover, the progress in the novel growth techniques, such as the development of the flow-rate modulated beam epitaxy, has made it possible to grow high-quality semiconductor heterostructures even from heavily lattice-mismatched materials, up to 7%, if the strained slabs are kept sufficiently thin. Besides the standard effects of bulk band discontinuity and slab thicknesses, the strain has indeed added a new degree of freedom to the growth technology to be explored in tailoring the heterostructure's bandgap.

[3] Present address: Physics Department, UAE University, PO Box 17551, Al-Ain, United Arab Emirates.

On the experimental side, strained-layer CdTe/ZnTe superlattices (SLs) have been grown for the first time by Monfroy *et al* [2] using the molecular-beam epitaxy (MBE) technique. This group characterized their samples by electron and x-ray diffraction and, despite the large mismatch between CdTe and ZnTe ($\Delta a/a \simeq 6.4\%$, named Δ hereafter), they claimed success in growing SLs of high quality. Subsequently, other growth techniques, such as metal–organic chemical vapour deposition (MOCVD) [3], have also been reliably used for successful growth of the same kind of SLs. However, whatever the advances achieved in the growth conditions, the misfit dislocations inevitably still occur in the experimental SLs as they are beyond the control of the growth techniques, and the sources of the limitations are mainly due to the elastic properties of the SL constituent materials. As a matter of fact, for any arbitrarily small lattice mismatch ($\Delta \geqslant 0.3\%$) between the buffer and the overlayer, there always exists a critical layer thickness d_c beyond which the misfit dislocations appear in the sample. With this aim, Miles and co-workers [4] have used photoluminescence (PL) and *in situ* reflection high-energy electron diffraction (RHEED) measurement to draw a map of d_c versus Δ for the strained $Cd_xZn_{1-x}Te/Cd_yZn_{1-y}Te$ common-anion SLs [4]. Many of these experiments have demonstrated that the substrates do not play a crucial role in controlling the character of the grown SLs, because due to the misfit dislocations the lattice constant jumps to that of a free-standing SL structure. In fact, one of the aims of the present work is to investigate the structural quality of the experimental SLs. This by itself is of essential importance as these particular SLs have potential for applications to optoelectronics such as intense visible light emitters.

On the theoretical side, several computational techniques have been used but were limited either by the system size and applicability only to the ground state properties, as in the first principles methods, or the complete neglect of the band mixing effects, as in the effective-mass approach (based on the Kronig–Penney model) or the Hückel method. To overcome such difficulties, we have used the sp^3s^* tight-binding (TB) method with inclusion of spin–orbit interaction, which are crucially important in the case of II–VI materials. The TB method has proven its reliability to successfully simulate the experimental data while it incorporates the microscopic description of the material, where the point group symmetry of the system is included. Within the Slater–Koster scheme [5], the TB method uses a small basis set of atomic orbitals and this gives the method the ability to deal with large systems; meanwhile it takes account of the band-mixing effects which are essential in the band structures of systems like quantum dots, wires, SLs and quantum wells. Consistent with this, one of the striking features of II–VI common-anion SLs is a vanishing or very small valence-band offset (VBO). This makes the mixing of valence bands (VBs) essential and the interplay between the biaxial strain and the vanishing VBO is of interest in its own right. Furthermore, it is worth mentioning that, in zinc-blende bulk semiconductors, the VB maximum is located at the Γ-point and is four-fold degenerate (including spin). Under the effect of biaxial strain as in the case of SLs, this degeneracy is further lifted by splitting the heavy-hole (HH: $M_J = \pm\frac{3}{2}$) and the light-hole (LH: $M_J = \pm\frac{1}{2}$) bands. Thus zero VBO in an unstrained case transforms into a finite VBO in the strained case. Confinement and band-mixing effects may thus compete with strain effects. Hence, the CdTe/ZnTe SLs should be a good condidate to follow the evolution of the electronic structure as a function of the SL layer thicknesses, VBO and strain configuration.

For all the reasons mentioned above, we have employed the sp^3s^* TB method, with inclusion of spin–orbit coupling and strain effects, to investigate the electronic properties of the strained CdTe/ZnTe(001) SLs. It is worth mentioning, here, that in the literature several attempts have been made to incorporate the strain effects within the TB Hamiltonian [6–14]. More specifically in the case of mismatched SLs, the biaxial strain results mainly in two structural distortions: (i) bond-length distortion and (ii) angular distortion. The former

distortion is usually described by scaling the *off-diagonal* energy elements (i.e. the overlap integrals) according to the famous Harrison $1/r^2$ rule, or another functional rule such as that of Priester *et al* [15]. However, in the TB framework, this particular distorsion cannot lift the degeneracy of the HH and LH states at the Brillouin-zone (BZ) centre (Γ-*point*), but it rather shifts the band edges. On the other hand, the second distortion affects the bond-directional cosines (l, m, n) which make the p_x, p_y and p_z orbitals asymmetrically contribute to the TB Hamilonian. As a consequence, in the presence of biaxial strain, the LH–HH degeneracy at the Γ-point must be lifted [14] if the Hamiltonian is expressed in the Slater–Koster scheme [5] with the minimal sp^3 basis set and in neglect of spin–orbit interaction. A subsequent development of this model is the addition of an excited s^* state to this latter basis set by Vögl *et al* [16]. The sp^3s^* models were essential especially for semiconductor materials, as they not only yield band dispersions in good agreement with those obtained by the state-of-art methods but rather they accurately reproduce the experimental bandgaps, carrier effectives masses and deformation potentials [7, 16, 17]. Even prior to this work, Kobayashi *et al* [18] had proposed a TB scheme which not only adds the s^* orbital to the sp^3-basis set but rather incorporates the idea [19] of the inclusion of the spin–orbit interactions, which are crucially important in the case of II–VI compound semiconductors. The overlap integrals, in this new ten-orbital/site-basis set, are carried up only to nearest neighbours. We recall that the point-group symmetry of the unstrained zinc-blende structure is T_d and, in the presence of the spin–orbit interaction, the upper VBs are formed by fourfold degenerate Γ_8 states, $|E^o_{v2}\rangle = |\frac{3}{2}, \pm\frac{3}{2}; v\rangle$ and $|E^o_{v1}\rangle = |\frac{3}{2}, \pm\frac{1}{2}; v\rangle$ (usually labelled HHs and LHs respectively), and twofold degenerate Γ_7 split-off (SO) states, $|E^o_{v3}\rangle = |\frac{1}{2}, \pm\frac{1}{2}; v\rangle$. However, in this latter model in the presence of biaxial strain, the LH–HH degeneracy at the Γ-point cannot *numerically* be lifted because the directional cosines (l, m, n) alter the Hamiltonian only through the phase shifts $\exp(i\boldsymbol{kr})$; and this latter factor has a vanishing effect on the Hamiltonian at the Γ-point ($\boldsymbol{k} = \boldsymbol{0}$). In an attempt to sort out this problem, Priester *et al* [7] used a self-consistent TB technique where the diagonal elements are variationally shifted along the growth direction as a consequence of charge redistribution due to the strain effect. Other authors [10, 11] used a version of the surface Green-function matching method adapted to strained SLs. They obtained that the splitting between LH and HH states is linearly proportional to the strain. More recently, however, Bertho *et al* [9] proposed a new scheme to incorporate the strain effects in the sp^3s^* TB Hamiltonian with the inclusion of the spin–orbit interactions. They treated the strain as a perturbation *posteriorly* added to the TB Hamiltonian (see next section for more details). As an effect of the reduced symmetry, in this latter scheme, the perturbation takes care of the interaction between all the states which belong to the same irreducible representations of the tetragonal point group D_{2d}. The main result of this work [9] is that the biaxial strain may cause the upper-conduction and valence interband mixing which, in turn, induces a non-linear splitting of LH and HH states at the Γ-point. The hydrostatic band mixing contributes to the non-linear behaviour of the band edges in high-pressure experiments and is one of the reasons for the sublinear pressure dependence observed for the fundamental bandgap $E_g(P)$ in III–V and II–VI materials [9]. The mixing effect demonstrates the complex hybridization mechanism of barrier-related and well-related states for building resonant-state wavefunctions in SLs. This idea of strain-induced band mixing has been corroborated by several experimental works. For instance, the evolution of the high-energy part of the reflectivity spectra versus the uniaxial stress in the $Ga_xIn_{1-x}As$/GaAs SLs has been well interpreted using this new TB scheme [20]. The same model also yields an HH–LH splitting variation with P in excellent agreement with the optical transitions of the PL experiments [6–9, 21]. Finally, we mention that this method of incorporating the strain in the TB Hamiltonian may exhibit electronic properties impossible to describe using the standard envelope-function approach and the usual deformation potential theory.

In this present work, we have adapted the same formalism [9] of incorporating the strain within the sp^3s^* TB scheme in the presence of spin–orbit coupling. We calculated the band structures of the CdTe/ZnTe(001) SLs versus the biaxial strain, layer thicknesses and VBO. This paper is organized as follows: in section 2, within this scheme, we give a brief description about the calculations of the electronic band structure and density of states. Section 3 illustrates a detailed discussion of our obtained results. Special emphasis is given to the effect of VBO on the electronic properties of SLs and, as applications, our results are compared to the PL experiments. The last section summarizes our conclusions.

2. Computational details

Within the TB framework, with inclusion of spin–orbit coupling and absence of strain, the electronic wavefunction is expressed in terms of a basis of symmetrically orthogonalized atomic orbitals $|b, \mu, \boldsymbol{R_i}\rangle$, also called the Löwdin orbitals [22]. Here $\boldsymbol{R_i}$ denotes a Bravais lattice point referred to the primitive cell, b is a basis atom in this primitive cell and μ denotes an orbital (such as $|s, \frac{1}{2}\rangle$, $|s, -\frac{1}{2}\rangle$, ... etc, which include the spin–orbit coupling) on atom b. The Hamiltonian is usually expressed [18] in terms of a basis $|b, \mu, \boldsymbol{k}\rangle$, which is obtained via a discrete Fourier transformation of the localized orbitals $|b, \mu, \boldsymbol{R_i}\rangle$, and given by

$$|b, \mu, \boldsymbol{k}\rangle = \frac{1}{\sqrt{N_w}} \sum_j \mathrm{e}^{\mathrm{i}\boldsymbol{k}\boldsymbol{R}_j} |b, \mu, \boldsymbol{R}_j\rangle \tag{1}$$

where N_w is the number of $\boldsymbol{k}$-vectors taken either from within the irreducible wedge of the BZ if the density of states is calculated, or along the high-symmetry lines if the band structure is evaluated.

The Schrödinger equation, whose solutions are the Bloch functions $|n\boldsymbol{k}\rangle$, is given by

$$(H_o - E_{n\boldsymbol{k}})|n\boldsymbol{k}\rangle = 0 \tag{2}$$

where H_o is the Hamiltonian of the system with inclusion of spin–orbit coupling. Equation (2) can be expressed in terms of the Löwdin basis set as

$$\sum_{j,\nu} [\langle i, \mu, \boldsymbol{k}|H_o|j, \nu, \boldsymbol{k}\rangle - E_{n\boldsymbol{k}}\delta_{i,j}\delta_{\mu,\nu}]\langle j, \nu, \boldsymbol{k}|n\boldsymbol{k}\rangle = 0 \tag{3}$$

where $E_{n\boldsymbol{k}}$ is the eigen-energy corresponding to the eigen-function $|n\boldsymbol{k}\rangle$, n is a band index, i and j denote basis atoms and μ and ν denote orbitals on these latter respective atoms. The Hamiltonian of either the bulk fcc or the SL structure uses the empirical TB parameters given in table 1. The CdTe parameters are due to [18] whereas the ZnTe parameters are due to [23]. These two respective sets of parameters yield the energy bandgap values of 1.59 and 2.39 eV, which are in excellent agreement with experimental values [24]. Moreover, the band dispersions possess carrier effective masses and deformation potentials in compatible agreement with experiments.

In the case of the presence of strain, such as in the SL structure, the strain is treated as a pertubation *posteriorly* added to the Hamiltonian [9]. In order to make this present paper self-contained, we briefly summarize the process of making this correction in the appendix.

One further remark about the heterostructure calculation is that the VBO is considered as a constant, and added to the *diagonal* elements of the overlayer (i.e. to one of the two materials in the case of SL structure; for instance added to the ZnTe slabs in our present case).

The obtained energy spectrum $E_{n\boldsymbol{k}}$ and corresponding wavefunctions $|n, \boldsymbol{k}\rangle$, from equation (3), are used to calculate the following quantities:

Table 1. The empirical sp^3s^* TB parameters, with inclusion of spin–orbit coupling, for CdTe and ZnTe, in units of electron volts. The same notation as in [18] is used. The lattice constants (a_0) are in Å units.

Compound	a_0	E_s^a	E_p^a	E_s^c	E_p^c	$4V_{ss}$	$4V_{xx}$	$4V_{xy}$
CdTe	6.48	−8.891	0.915	−0.589	4.315	−4.779	2.355	4.124
ZnTe	6.08	−9.190	0.627	−1.420	3.779	−6.642	1.940	4.077
Compound	$4V_{sp}^{ac}$	$4V_{ps}^{ac}$	$E_{s^*}^a$	$E_{s^*}^c$	$4V_{s^*p}^{ac}$	$4V_{ps^*}^{ac}$	λ_a	λ_c
CdTe	1.739	−4.767	7.0	7.5	1.949	−2.649	0.367	0.013
ZnTe	5.925	−4.673	6.227	6.779	2.962	−3.827	0.362	0.027

(i) the total density of states (TDOS) given by

$$N(E) = \frac{1}{N_w}\sum_{n,\boldsymbol{k}}^{N_w}\delta(E - E_{n\boldsymbol{k}}) \tag{4}$$

(ii) the local density of states (LDOS), due to the orbital μ on the atom b, given by

$$N_{b,\mu}(E) = \frac{1}{N_w}\sum_{n,\boldsymbol{k}}^{N_w}|\langle b, \mu, \boldsymbol{R_i}|n, \boldsymbol{k}\rangle|^2\delta(E - E_{n\boldsymbol{k}}) \tag{5}$$

(iii) the partial density of states (PDOS), due to the atomic species of type α (such as Cd, Zn, or Te atoms), given by

$$N_\alpha(E) = \sum_{b,\mu} N_{b,\mu}(E) \tag{6}$$

where the sum runs over all the orbitals of all the sites of type α.

We emphasize that the $\boldsymbol{k}$-space integration carried out in evaluating equations (4) and (5) is performed using the Monkhorst–Pack technique [25], and the δ-function is numerically approximated by a Gaussian:

$$\delta(x) = \frac{1}{\sigma\sqrt{2\pi}}\exp\left[-\frac{x^2}{2\sigma^2}\right] \tag{7}$$

of width $\sigma = 0.05$ eV. All of the TDOSs are normalized to ten electrons (i.e. one zinc-blende molecule). The results of our calculations are presented in the next section.

3. Results and discussions

3.1. Fcc bulk bandstructure

In figures 1 and 2, we display the electronic band structures of bulk CdTe and bulk ZnTe respectively. These results were obtained using the 20-band (sp^3s^* with inclusion of spin degeneracy) model whose parameters are given in table 1. The top of the VB is chosen as an energy reference. The energy gaps obtained are *direct* and of values $E_g = 1.59$ and 2.39 eV for CdTe and ZnTe respectively, which are the same as the experimental values [24]. The irreducible representations corresponding to the point-group symmetry of the eigenfunctions are also shown in figures 1(a) and 2(a) for the high-symmetry points Γ and X of the BZ. In both of these latter panels, the lowest group is dominated by contribution from the s orbitals of anion (Te) atoms. The second group, which is the VB, consists of the cationic s states and all the p states. For CdTe (figure 1), the VB and CB have bandwidths of values 5.3 and 7.2 eV respectively, whereas the bandwidths of the VB and CB of ZnTe (figure 2) are 5.8 and 7.2 eV respectively. Here, it is worth mentioning the following two quantitative trends.

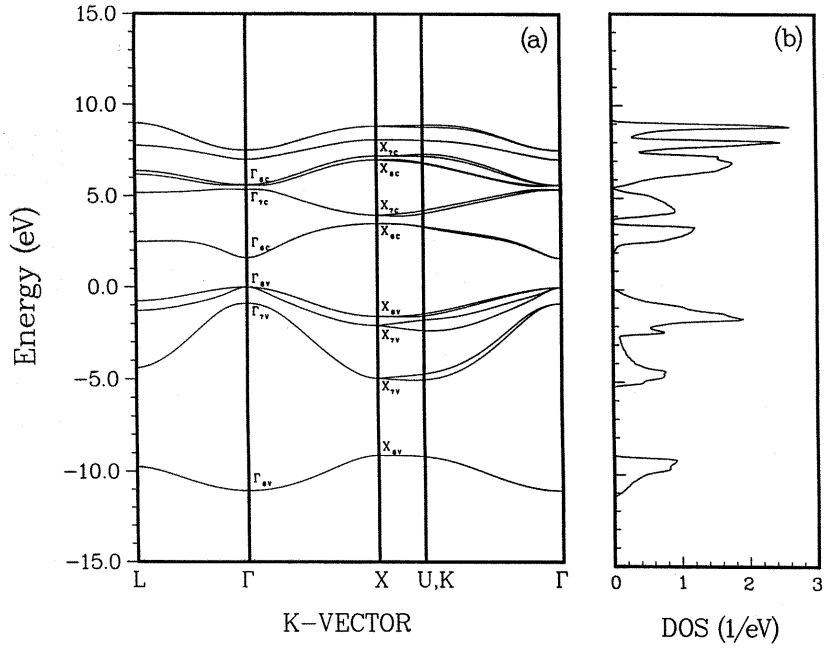

Figure 1. The electronic structure of fcc bulk CdTe calculated using the sp^3s^* TB model, with the inclusion of spin–orbit coupling: (a) the energy bands; (b) the density of states. The top of the VB is taken as an energy reference and the DOS is normalized to ten electrons.

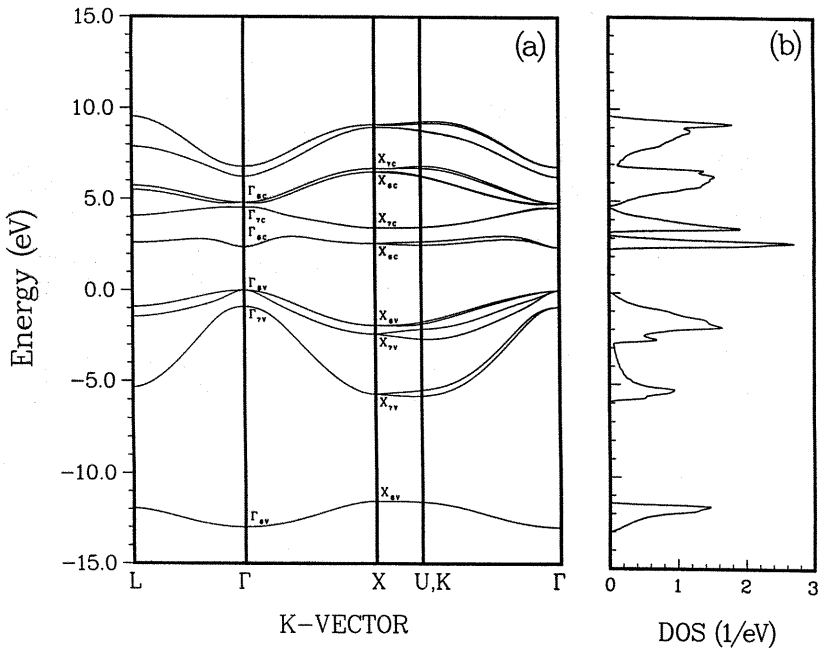

Figure 2. The same as figure 1, but for fcc bulk ZnTe.

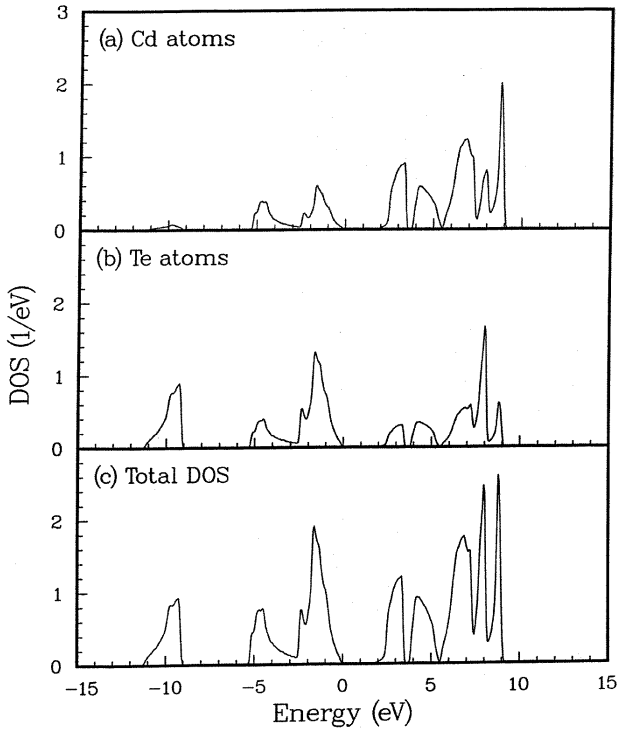

Figure 3. PDOS contributions from orbitals on (a) Cd atoms and (b) Te atoms to (c) the TDOS of pure CdTe. TDOS is normalized to ten electrons.

(i) In general, as the lattice constant decreases, the VB width increases (compare figures 1(b) and 2(b)). This can be ascribed to a reduction of hybridization with increasing separation of the atomic constituents. Moreover, predominantly ionic materials have wider VB than do predominantly covalent materials.

(ii) The other trend is that the optical gap in common-anion (or cation) semiconductors decreases with the heavier cation (or anion).

The third group of bands, which form the conduction band (CB), are mainly due to contributions from the p and s* orbitals.

In figure 3, we display the total and partial densities of states for CdTe, which more likely would play the role of well in the SLs. Similar trends are observed for ZnTe. As can be seen in panels 3(a) and (b), Cd and Te atoms experience the same point-group symmetry (T_d) and, as a consequence, they have very similar splittings and LDOS profiles. One also may notice that the first group of bands consists mainly of Te atom contributions. Furthermore, Te atoms contribute to the VB with a weight bigger than that of Cd atoms. These latter atoms contribute more to the CB structure. This, indeed, reflects the fact that CdTe is a polar material with a partial ionic character.

In figure 4, we decompose the TDOS into PDOSs due to (a) all the s* orbitals, (b) all the s orbitals and (c) all the p orbitals. It is clear that the s* orbitals contribute only to the CB and predominantly to the higher conduction bands. By taking the superposition of figures 3 and 4, it should be clearly seen that the first group is mainly due to the anionic s orbitals. Furthermore, figure 4 shows that the VB and CB are due to an admixture of all s and p orbitals in the hybridization process and, therefore, again reflect the covalent character of CdTe.

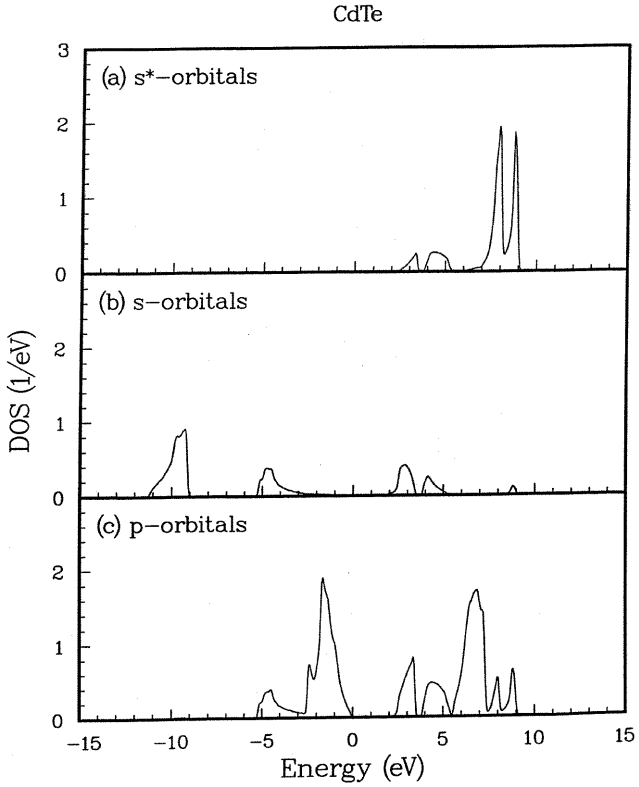

Figure 4. Orbital density-of-states contributions from (a) s* orbitals, (b) s orbitals and (c) all the p orbitals to the TDOS of pure bulk CdTe.

3.2. Strained bulk bandstructure

The purpose here is to put under the scope the strain effects as a component separated from the global band offset problem. Of course, the biaxial strain significantly affects the level splittings at the top of the VB. In this section, we aim to discuss the strain effects on the VBO in each of the bulk materials under the same strained configuration corresponding to the structure of the SL, eventually to be studied.

As mentioned in the last section, the strain has been treated as a perturbation *posteriorly* added to the TB Hamiltonian. Besides this, the off-diagonal TB parameters have been scaled according to Priester's rule [15] in order to take account of the bond-length distorsion due to the strain. The results for CdTe and ZnTe are shown in figures 5(a) and (b) respectively. The calculation has used a tetragonal unit cell of four atoms whose in-plane lattice constant has been varied from 6.08 Å (of cubic ZnTe) to 6.48 Å (of cubic CdTe). The inter-plane lattice constant has been calculated using the macroscopic theory of elasticity (MTE) [24]. Since both materials possess direct bandgaps, we have assessed the level splittings only at the Γ-point. The energy reference has been taken to be the VB edge of either material in its unstrained fcc-bulk structure.

Now, in the strained SLs, the biaxial strain is *tensile* for ZnTe and *compressive* for CdTe. Figure 5 shows the variation of the energies of the top VB states (namely the spin-off (SO) state represented by $\circ$, the HH state represented by $\diamond$ and the LH state represented by $\triangledown$) and

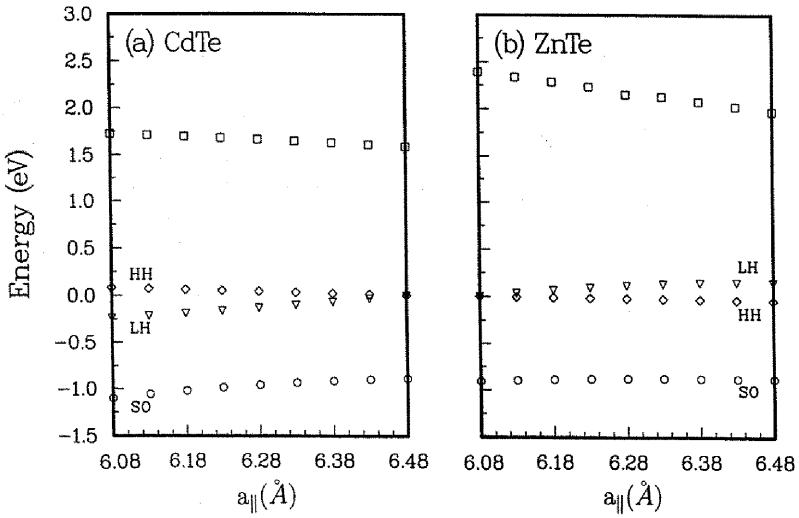

Figure 5. Energy variation of the lowest CB state and the top VB states (HH, LH and SO) under the effect of the biaxial strain. (a) CdTe under *compressive* strain; (b) ZnTe under *tensile* strain.

the lowest CB state, denoted by □, versus the strain (i.e. the in-plane lattice constant $a_{\|}$). The E_g of CdTe seems to be insensitive under the *compressive* strain, contrarily to the E_g of ZnTe which decreases under the *tensile* strain. This is consistent with the contrast in bandgaps which we have drawn between figures 1 and 2. It seems to be a real fact that if the cation (or anion) atom is substituted by a larger atom the E_g reduces. In the case of CdTe (figure 5(a)), the HH lies above LH when a *compressive* strain is applied. On the other hand, the LH lies above the HH when a *tensile* strain is applied on ZnTe (figure 5(b)). The maximum splitting energy between HH and LH is 0.32 and 0.19 eV for CdTe and ZnTe respectively. The non-linearity of the splitting is clearly seen in the behaviour of the SO state and does have experimental evidence for it [26].

Another significant effect of the biaxial strain is that it alters the orbital character of the electronic states and, therefore, affects the optical properties. The CB edge persists always in being s-like and the HH state maintains equal strengths in p_x-like and p_y-like characters. In contrast, the LH and SO states, with a varying admixture of p orbitals, undergo a substantial change in the relative proportion of strengths as strain increases. For instance, the LH in the strained CdTe becomes almost p_z-like while the SO state becomes more $p_{x,y}$-like with very small fraction of p_z-like character. Thus, the strain has very significant effects on the spectral properties of the VB edge states, as it changes substantially the orbital character.

3.3. Superlattice bandstructure

In the SL calculations, two assumptions are considered:

(i) the heterostructure is pseudomorphic (defect-free) and
(ii) the MTE is valid in predicting the SL atomic structure.

Therefore, despite the large lattice mismatch (∼6.4%), the thickness of each slab is assumed to be below the critical thickness (d_c) corresponding to the appearance of the misfit dislocations. In real life, these latter inevitably occur in the experimental samples and will be the subject of the next section.

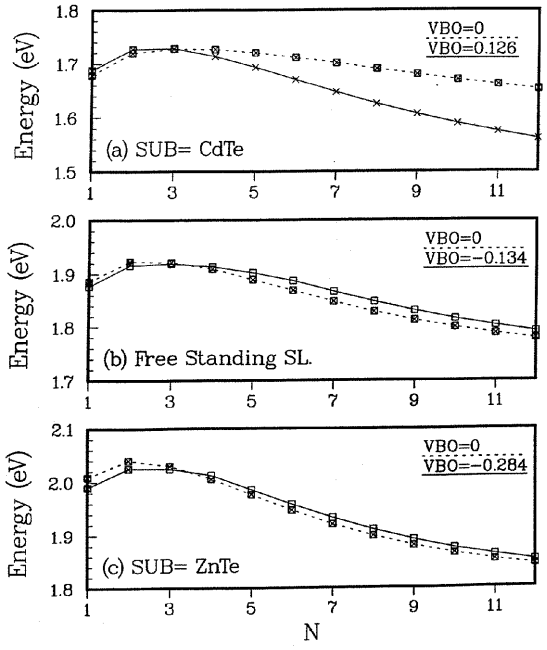

Figure 6. The variation of the energy gap of the $(CdTe)_n(ZnTe)_n(001)$ SL versus n. Each panel represents one biaxial strain state. Two extreme values of VBOs are considered for each panel. The character of the SL is indicated by the shown symbols (see the text for details).

To map the strain effect, we have chosen to work on three differently strained SLs, two among which are the ones extremely strained to either CdTe substrate (figure 6(a)) or ZnTe substrate (figure 6(c)). The third one is the free-standing SL and is chosen as its strain state lies in between (a) and (c) and, meanwhile, is of crucial importance for physical applications. Of course, within the TB framework, to calculate the SL bandstructure, one must take into account the band offsets. As mentioned in the last section, the VBO is considered as a constant and added to the diagonal elements of the Hamiltonian matrix. Namely, we have added $\mathrm{VBO} = E_v(\mathrm{ZnTe}) - E_v(\mathrm{CdTe})$ to the on-site elements of the ZnTe slabs. Here, E_v is the VB edge of the material, shown in brackets, under the strained configuration corresponding to the SL structure. In figure 6, two extreme VBO values are considered for each strain state and are displayed on each panel. As it is a well known fact that the II–VI common-anion SLs possess vanishing or very small VBO, we took $\mathrm{VBO} = 0$ as one of our choices. The second VBO value, which is a kind of overestimate, is due to the model-solid approach of Van de Walle [24]. To the best of our knowledge, all the VBOs found in the literature, lie in between these two extremes. In addition to the strain state and the VBO, the third parameter controlling the SL bandstructure is the slab thickness. In figure 6, we have chosen to investigate the $(CdTe)_n(ZnTe)_n(001)$ strained SLs, where both slabs have the same number of monolayers. Since both materials possess direct bandgaps, we have just used the Γ-point to calculate the energy gap (E_g) versus layer thickness (n). We found that the electron is always confined within the CdTe slab. Hence, the SL character is fully determined by the hole behaviour. In figure 6, for each specific strain state and specific VBO value, and particular slab thickness (n), the SL is characterized by one of three symbols:

(i) the symbol □ denotes the SL of type I, where the SL VB edge consists of the HH which is confined in the CdTe slab;

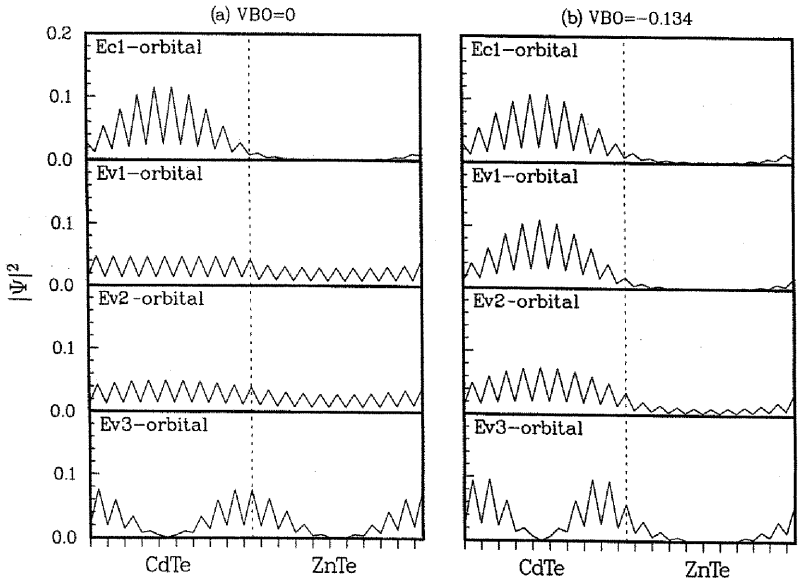

Figure 7. The calculated wavefunction squared amplitudes for the free-standing $(CdTe)_{10}(ZnTe)_{10}(001)$ SL using (a) VBO = 0 and (b) VB = −0.134 eV. Ec1 corresponds to the lowest CB electron state, whereas Ev1, Ev2 and Ev3 correspond to the three highest VB hole states.

(ii) the symbol × denotes the SL of type II, where the LH localized within the ZnTe slab consists of the SLs VB edge;

(iii) the symbol of crossed □ stands for an SL that is not well characterized as the VB-edge hole is extended over the whole SL slabs.

As shown in the three panels of figure 6, the variation of strain causes the increase in the E_g when the substrate lattice constant is reduced from that of CdTe to that of ZnTe. Furthermore, the strain does have an effect on the character of the SL as it enhances the admixture of the p_x, p_y and p_z orbitals as described in the previous section.

In figure 6(a), the VBO has a positive sign and, therefore, makes the VB edge of ZnTe higher than that of CdTe. This yields an SL of type II, which seems to be more sensitive to the variation of VBO especially for large n as the confinements of the electron and the hole are completely independent. On the other hand, in figures 6(b) and (c), the VBO is negative and yields an SL of type I. The SL E_g seems not to be too sensitive to the variation of VBO because both the electron and the hole are localized in the CdTe slab and there exists a compromise in their confinement characters. Now, we discuss the E_g versus n. Of course, it is evident that the variation of E_g tends toward the $E_g(\mathrm{CdTe}) = 1.59$ eV when n is very large as an effect of confinement and this explains the reduction of E_g as n increases. For small values of n, however, E_g seems to increase and has a maximum value when $n = 2$ then starts its decrease. This may be interpreted as a strong band mixing occurring within the VBs.

In figure 7, we display the behaviours of the wavefunctions, calculated at the Γ-point, corresponding to the electron and upper hole states of the CB and VB respectively. The *abscisa* axis represents the c-direction of the SL, and the *ordinate* axis gives the variation of the planar-averaged squared amplitude of the wavefunction. Figure 7 shows the results for a free-standing $(CdTe)_n(ZnTe)_n$ (001) SL, with $n = 10$, for two cases of VBO: (a) VBO = 0 eV, and

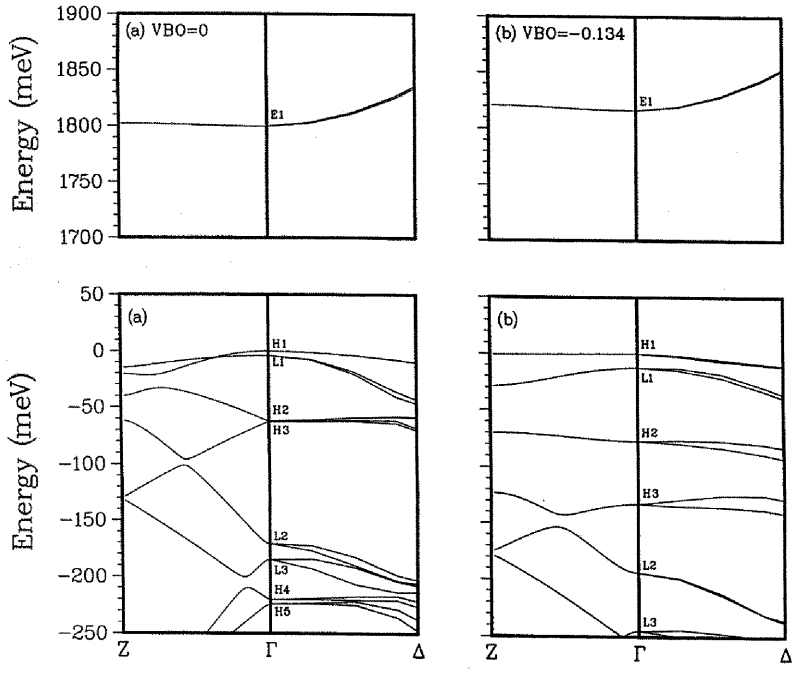

Figure 8. Electronic band structures for the case of the free-standing $(CdTe)_{10}(ZnTe)_{10}(001)$ SLs calculated with (a) VBO = 0 and (b) VBO = −0.134 eV. In both panels, the SLs VB edge is taken as an energy reference.

(b) VBO = −0.134 eV. Actually, these two cases correspond to two data points in figure 6(b). It can clearly be seen that the electron (Ec1) is always localized within the CdTe slab. For VBO = 0 the hole (Ev1) is delocalized along the whole SL, whereas for VBO = −0.134 the top hole (HH) gets confined within the CdTe region and, therefore, yields a SL of type I. The final remark about figure 7 is that the third hole state (Ev3) is found to have a tendency to localize at the interface when VBO is vanishing. The same observation was also reported by Quiroga *et al* [12] and just reflects the strong mixing effects occurring within the VBs.

Figure 8 displays the band structures of the two SLs previously discussed in figure 7, which are the free-standing SLs with $n = 10$ and (a) VBO = 0 eV and (b) −0.134 eV. In both, the SL valence bandedge is considered as an energy reference and the lowest CBs as well as upper VBs are shown. The $\boldsymbol{k}$-vector is varied along the ZΓ line and along one portion of the ΓX line of the BZ. The ZΓ line is, effectively, sufficient to give a prediction about the confinement state of charge carriers. It is obvious that the electron in both panels (a) and (b) is localized with respect to the c-axis, as its conduction band is flat along the ZΓ line. The HH state (H1) is also localized within CdTe when VBO = −0.134 eV and this is also shown by the nesting H1 band in panel (b) along the ZΓ line.

Figure 9 presents the variation in energy of the two upper VB states, calculated at the Γ-point, versus VBO. These results are shown for the free-standing $(CdTe)_{10}(ZnTe)_{10}(001)$ SL. We emphasize the following observations.

(i) For a free-standing SL made up of two semiconductor materials having the same number of monolayers n, the *in-plane* lattice constant should be independent of n ($a_{\parallel} = 6.238$ Å). The variation of n only changes the confinement energy.

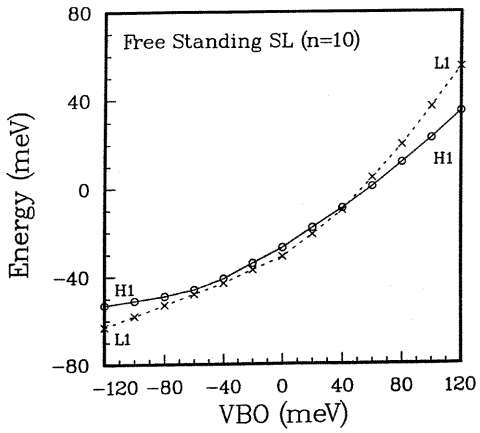

Figure 9. Variation of the two highest-energy VB states versus VBO, for the free-standing $(CdTe)_{10}(ZnTe)_{10}(001)$ SL.

(ii) For the considered range of VBOs, the electron is always localized within the CdTe slab.
(iii) H and L denote the nature of the SL states at the zone centre according to whether, mainly or wholly, they originate from the bulk heavy- or light-hole states.

The valence states are strongly dependent on VBO. When VBO $= 0$, CdTe is the well material for the HH state and the SL is of type I. For negative VBO values, the localization of the HH state (H1) in CdTe layers increases and the bandgap is reduced. The LH state L1 remains extended and lower than H1 in energy. The case of positive values of VBO presents more interesting features and gives evidence for a SL type I to type II transition. The increase of VBO lowers the barrier height for the HH which becomes extended in the whole SL and increases the localization of the LH state, which becomes the SL hole ground state. So, VBO $\simeq 40$ meV appears as the value for which the transition occurs. For VBO > 40 meV, the LH state (L1) lies above the HH state (H1) and the SL is of type II. The exciton transition becomes *indirect* in real space with an expected weak oscillator strength [27].

3.4. Modelling of photoluminescence experiments

The first PL measurements, for the CdTe/ZnTe SLs, were reported by Miles *et al* [28]. The grown SLs displayed intense visible PL spectra, which made the systems promising devices for light sources and photo-detectors. As mentioned in the introduction, the same research group [2] was the first to report a successful growth of high quality of the same type of SLs. In their samples, CdTe layers varied in thickness between 20 and 49 Å, while ZnTe barriers were between 20 and 51 Å wide. The SLs were grown on either (001)CdTe, ZnTe or $Cd_xZn_{1-x}Te$ buffer layers. The experimental results of PL measurements (at 5 K) done on various samples are summarized in table 2. On the other hand, in our computation, we have assumed a pseudomorphic SL structure and used the MTE [24] to fit the experimental structural data. Furthermore, the validity of MTE is assumed even in the ultimate limit of one nominal strained monolayer. In our theoretical work, the VBO is taken as a free parameter to be adjusted to yield the exact E_g as obtained in the PL experiments. The results of our TB method, which includes spin–orbit coupling, are also summarized in table 2 for the sake of comparison. We emphasize that these theoretical results correspond to the free-standing SL case, and that the E_g values are much lower than experimental data if one took the same

Table 2. The theoretical VBO, shown here, is for the case of the free-standing $(CdTe)_m(ZnTe)_n(001)$ SL and corresponds to exactly fitting the experimental E_g. Theoretically, the numbers of monolayers m and n are determined using the MTE [24].

Sample	Superlattice[a] (CdTe/ZnTe) (Å)	Buffer layer[a]	E_g (eV)[a,b]	VBO (meV)[b]
1	25/35	CdTe	1.87	6
2	28/21	CdTe	1.81	6
3	51/50	CdTe	1.69	86
4	27/30	ZnTe	1.81	46
5	21/30	$Cd_{0.5}Zn_{0.5}Te$	1.83	116
6	26/33	$Cd_{0.5}Zn_{0.5}Te$	1.82	41
7	34/36	$Cd_{0.5}Zn_{0.5}Te$	1.74	86
8	22/18	$Cd_{0.5}Zn_{0.5}Te$	1.78	176

[a] Experimental data due to [28].
[b] Present work.

Table 3. Same as table 2 but for the experimental data corresponding to [29] where the buffer is ZnTe and the theoretical VBOs correspond to SLs of ZnTe substrate as well.

Sample	Superlattice[a] (CdTe/ZnTe) (Å)	E_g (eV)[a,b]	VBO (meV)[b]
1	9/40	2.24	−84
2	12/40	2.15	−49
3	24/40	1.82	136
4	40/40	1.74	121

[a] Experimental data due to [29].
[b] Present work.

experimental buffer. Furthermore, the VBO has a reverse effect on the SL E_g (i.e. the SL E_g reduces with the increase of VBO). Our theoretical results predicts that the top VB state is either extended or an LH localized within the ZnTe slabs; and hence favours more the character of SLs of type II. Therefore, it seems that the distribution of strain between CdTe and ZnTe layers is difficult to modulate through the choice of substrate as the large lattice mismatch causes a rapid relaxation and the lattice constant of the SL jumps into the one of a free-standing SL as soon as the primary misfit dislocation appears. Obviously, the strain distribution (*morphology*) plays a crucial role in determining the SL bandgap and character.

More recent PL experimental data are due to Kuwabara *et al* [29]. The CdTe/ZnTe strained-layer SLs are grown on ZnTe buffer layer, using hot-wall epitaxy (HWE). The cross-sectional transmission electron microscopy (TEM) image shows that the critical thickness of the CdTe well layer is about $d_c \simeq 12$ Å. The experimental results of the picosecond time-resolved PL spectra are shown in table 3. Our theoretical TB results are also shown for SLs strained to ZnTe substrate for comparison. The VBO is varied to yield the same E_g as in the experimental data. In table 3, the theoretical results show that the SLs 1 and 2 are of type I because their corresponding VBO is less than the critical value of 30 meV (which is calculated for the case of SLs strained to ZnTe substrate). The other SLs are of type II. This, indeed, is consistent with TEM predictions [29] as the thickness of the CdTe well is less than the critical value d_c in the case of SLs 1 and 2. Hence, our TB results suggest that the strain is no longer confined in the CdTe slabs in the case of samples 3 and 4. We emphasize, here, that this is not a problem related to the growth technique but rather it is an intrinsic effect related to the elastic properties of the SL constituents.

4. Conclusions

We have used the sp^3s^* TB method, with inclusion of spin–orbit coupling, to investigate the electronic properties of the strained CdTe/ZnTe(001) SLs. Within the TB scheme, we have calculated the SL band structure and various densities of states versus the strain state, layer thicknesses and band offsets.

Since the II–VI semiconductor heterostructures are expected to have either vanishing or small VBOs, the biaxial strain plays an essential role in determining the SL character as it controls the splittings of the top VB states. We have deconvoluted the band offset problem into separable components. The first one we could separate is the biaxial strain effect. From a computational point of view, within the TB framework, the strain has been treated as a perturbation *posteriorly* added to the Hamiltonian. The results have shown that the top VB state is HH-like for CdTe under *compressive* strain, and is LH-like for ZnTe under *tensile* strain.

In the calculation of the strained SLs, the electron is found to be always confined within the CdTe slabs, whereas the hole is sensitive to the VBO, and its behaviour controls the SL's character. Since the SL constituents are of relatively large lattice mismatch ($\sim$6.4%), misfit dislocations inevitably can occur in the grown experimental samples. For this reason, we have given special attention to the study of the free-standing SLs, which might be the limit case of the relaxed SL structure. The free-standing $(CdTe)_n(ZnTe)_n(001)$ SL is studied versus layer thickness (n) and VBO. Two extreme values of VBO, which correspond to a vanishing value and the one obtained using the model solid approach, are taken. The effect of n is shown to only control the degree (energy) of confinement in the CdTe well. The variation of VBO predicted the SL character to exhibit a type I to type II transition for a critical VBO value of about 40 meV. For VBO $<$ 40 meV, the HH is localized within the CdTe slabs and the SL is of type I. However, if VBO $>$ 40 meV, the LH localized within the ZnTe slab becomes the top SL VB state and therefore the SL is of type II.

The results of our work have been shown to be useful in interpreting the PL data. Mainly, they were used in determining the strain distribution and the SL character. Some valuable information regarding the structural and optical qualities of the SLs have also been drawn.

Acknowledgments

One of the authors (NT) would like to thank Professor Yu Lu for the invitation to visit the ICTP, as well as thank Professors J Chadi, C Dharma-wardana, C Priester and V Velasco for stimulating discussions. We thank Professor A Hamza for his critical reading of the manuscript. This work was supported by the Research Affairs at the UAE University under grant number 08-2-11/01.

Appendix

In the framework of the sp^3s^* TB, with the inclusion of spin–orbit interaction, the biaxial strain is incorporated into the Hamiltonian in a perturabative fashion as follows:

$$H = H_o + H_s(\varepsilon) \tag{A.1}$$

where H_o is the sp^3s^* TB Hamiltonian which includes the spin–orbit coupling effects and $H_s(\varepsilon)$ is the strain part which will be *posteriorly* added as a perturbation to the system. In this latter part, the interaction is switched on between eigenstates which belong to the same irreducible representations at the BZ centre (Γ-point). As far as the lowest CB states and the top VB states are concerned in the case of strained bulk material, the strain involves the

Table A.1. Intraband and interband hydrostatic and uniaxial deformation potentials (in eV) for both CdTe and ZnTe, due to [9].

Compound	a_v	a'_v	a_{cv}	a'_{cv}	b	b'	b_{cv}	b'_{cv}
CdTe	1.10	0.93	2.16	2.22	−1.20	−1.13	−2.47	−2.51
ZnTe	1.30	1.13	3.37	3.43	−1.20	−1.12	−3.11	−3.14

mixing between mainly six states (namely in figures 1(a) and 2(a): $|E^o_{v3}\rangle$ and $|E^o_{v1}\rangle$ with $|E^o_{v2}\rangle$ correspond to the SO and LH/HH states of the respective irreducible representations Γ_{7v} and Γ_{8v}; whereas $|E^o_{c3}\rangle$ and $|E^o_{c1}\rangle$ with $|E^o_{c2}\rangle$ correspond to the upper CB states of the respective irreducible representations Γ_{7c} and Γ_{8c}), which were obtained in the absence of strain.

For a biaxial strain, H_s can be linked with the deformation potential theory, and written as follows:

$$\begin{array}{c} \\ \langle E^o_{v2}| \\ \langle E^o_{c2}| \\ \langle E^o_{v1}| \\ \langle E^o_{v3}| \\ \langle E^o_{c1}| \\ \langle E^o_{c3}| \end{array} \begin{array}{c} \begin{array}{cccccc} |E^o_{v2}\rangle & |E^o_{c2}\rangle & |E^o_{v1}\rangle & |E^o_{v3}\rangle & |E^o_{c1}\rangle & |E^o_{c3}\rangle \end{array} \\ \begin{pmatrix} a_v\mathrm{Tr}(\varepsilon) - b\varepsilon_u & a_{cv}\mathrm{Tr}(\varepsilon) - b_{cv}\varepsilon_u & 0 & 0 & 0 & 0 \\ a_{cv}\mathrm{Tr}(\varepsilon) - b_{cv}\varepsilon_u & E'_c - a_v\mathrm{Tr}(\varepsilon) + b\varepsilon_u & 0 & 0 & 0 & 0 \\ 0 & 0 & a_v\mathrm{Tr}(\varepsilon) + b\epsilon_u & -\mathrm{i}\sqrt{2}b'\varepsilon_u & a_{cv}\mathrm{Tr}(\varepsilon) + b_{cv}\varepsilon_u & -\mathrm{i}\sqrt{2}b'_{cv}\varepsilon_u \\ 0 & 0 & \mathrm{i}\sqrt{2}b'\varepsilon_u & -\Delta_o + a'_v\mathrm{Tr}(\varepsilon) & \mathrm{i}\sqrt{2}b'_{cv}\varepsilon_u & a'_{cv}\mathrm{Tr}(\varepsilon) \\ 0 & 0 & a_{cv}\mathrm{Tr}(\varepsilon) + b_{cv}\varepsilon_u & -\mathrm{i}\sqrt{2}b'_{cv}\varepsilon_u & E'_c - a_v\mathrm{Tr}(\varepsilon) - b\varepsilon_u & -\mathrm{i}\sqrt{2}b'\varepsilon_u \\ 0 & 0 & \mathrm{i}\sqrt{2}b'_{cv}\varepsilon_u & a'_{cv}\mathrm{Tr}(\varepsilon) & \mathrm{i}\sqrt{2}b'\varepsilon_u & E'_o - a'_v\mathrm{Tr}(\varepsilon) \end{pmatrix} \end{array} \tag{A.2}$$

where ε is the strain tensor and $\varepsilon_u = (\varepsilon_\parallel - \varepsilon_\perp)/3$; a_v (a'_v) is the intraband hydrostatic deformation potential for the HH and LH states (the split-off states); a_{cv} is the interband hydrostatic deformation potential coupling the HH states E_{v2} (or LH states E_{v1}) to the conduction states E_{c2} (or E_{c1}); a'_{cv} is the interband hydrostatic deformation potential coupling the split-off states E_{v3} to the conduction states E_{c3}; b_v (b_c) describes the linear splitting of the valence $|E^o_{v1}\rangle$ and $|E^o_{v2}\rangle$ states (of the conduction $|E^o_{c1}\rangle$ and $|E^o_{c2}\rangle$ states); within the TB model $b = b_v = -b_c$; b' is related to the mixing of $|E^o_{v1}\rangle$ with $|E^o_{v3}\rangle$ in the VB and of $|E^o_{c1}\rangle$ with $|E^o_{c3}\rangle$ in the CB. b_{cv} describes the upper-conduction–valence mixing of $|E^o_{v1}\rangle$ with $|E^o_{c1}\rangle$ states and b'_{cv} is related to the upper-conduction–valence mixing of $|E^o_{v1}\rangle$ with $|E^o_{c3}\rangle$. We also recall that the eigen-energies of the pure bulk lattice are given by

$$E^o_{v1} = E^o_{v2} = 0,$$

$$E^o_{v3} = -\Delta_o = \frac{E^a_p - 2\lambda_a + E^c_p - 2\lambda_c}{2} - \frac{1}{2}\sqrt{(E^a_p - 2\lambda_a - E^c_p + 2\lambda_c)^2 + 4V^2_{xx}}$$

$$E^o_{c1} = E^o_{c2} = E'_c = E'_o + \Delta'_o = \frac{E^a_p + \lambda_a + E^c_p + \lambda_c}{2} + \frac{1}{2}\sqrt{(E^a_p + \lambda_a - E^c_p - \lambda_c)^2 + 4V^2_{xx}}$$

$$E^o_{c3} = E'_o = \frac{E^a_p - 2\lambda_a + E^c_p - 2\lambda_c}{2} + \frac{1}{2}\sqrt{(E^a_p - 2\lambda_a - E^c_p + 2\lambda_c)^2 + 4V^2_{xx}}$$

where E^a_p, E^c_p, λ_a, λ_c and V_{xx} are the TB parameters shown in table 1. The intraband and interband deformation potentials for both CdTe and ZnTe are summarized in table A.1 and they are due to the work by [9].

References

[1] For a review, see for instance
Bauer G and Krenn H 1991 *Contemp. Phys.* **32** 383
[2] Monfroy G, Sivananthan S, Chu X, Faurie J P, Knox R D and Staudenmann J L 1986 *Appl. Phys. Lett.* **49** 152

[3] Shtrikman H and Finkman E 1989 *Superlatt. Microstruct.* **6** 55
[4] Miles R H, McGill T C, Sivananthan S, Chu X and Faurie J P 1987 *J. Vac. Sci. Technol.* B **5** 1263
[5] Slater J C and Koster G F 1954 *Phys. Rev.* **94** 1498
[6] Bertho D, Boiron D, Simon A, Jouanin C and Priester C 1991 *Phys. Rev.* B **44** 6118
[7] Priester C, Bertho D and Jouanin C 1993 *Physica* B **191** 1
[8] Jouanin C, Bertho D and Benoit C 1993 *Phys. Rev.* B **47** 3706
[9] Bertho D, Jancu J M and Jouanin C 1994 *Phys. Rev.* B **50** 16 956
[10] Arriaga J, Munõz M C, Velasco V R and Garcia-Moliner F 1991 *Phys. Rev.* B **43** 9626
[11] Arriaga J and Velasco V R 1992 *Phys. Scr.* **46** 83
[12] Quiroga L, Camacho A, Brey L and Tejedor C 1989 *Phys. Rev.* B **40** 3955
[13] Wu Yi-hong, Fijita Shizuo and Fujita Shigeo 1990 *J. Appl. Phys.* **67** 908
[14] Lin-Chung P J and Yang M J 2000 *J. Appl. Phys.* **87** 4319
[15] Priester C, Allan G and Lannoo M 1988 *Phys. Rev.* B **37** 8519
[16] Vögl P, Hjalmarson H P and Dow J D *J. Phys. Chem. Solids* **44** 365
[17] Tit N 1997 *J. Phys.: Condens. Matter* **9** 6505
[18] Kobayashi A, Sankey O F and Dow J D 1982 *Phys. Rev.* B **25** 6367
[19] Chadi D J 1977 *Phys. Rev.* B **16** 790
[20] Boring P, Jancu J M, Gil B, Bertho D and Jouanin C 1992 *Phys. Rev.* B **46** 4764
[21] Bertho D, Jancu J M and Jouanin C 1993 *Phys. Rev.* B **48** 2452
[22] Löwdin P O 1950 *J. Chem. Phys.* **18** 365
[23] Olguin D and Baquero R 1995 *Phys. Rev.* B **51** 16 891
[24] Van de Walle C G 1989 *Phys. Rev.* B **39** 1871
[25] Monkhorst H J and Pack J P 1976 *Phys. Rev.* B **13** 5188
[26] Welber B, Cardona M, Kim C K and Rodrigues S 1979 *Phys. Rev.* B **12** 5729
[27] Tran M, Tit N and Dharma-wardana M W C 1999 *Appl. Phys. Lett.* **75** 4136
[28] Miles R H, Wu G Y, Johnson M B, McGill T C, Faurie J P and Sivananthan S 1986 *Appl. Phys. Lett.* **48** 1383
[29] Kuwabara H, Asai H, Tatsuoka H, Nakamura T, Nakanishi Y and Fujiyasu H 1996 *J. Cryst. Growth* **159** 839